Green Color Purification in Tb^{3+} Ions through Silica Inverse Opal Heterostructure

Vishnu Prasad Shrivastava,[†] Sri Sivakumar,*,[†,‡,§,⊥] and Jitendra Kumar*,[†]

[†]Materials Science Programme, [‡]Department of Chemical Engineering, [§]Centre for Environmental Science and Engineering, [⊥]Thematic Unit of Excellence on Soft Nanofabrication, Indian Institute of Technology Kanpur, Kanpur 208016, India

Ⓢ *Supporting Information*

ABSTRACT: The ordered SiO$_2$:Tb^{3+} inverse opal heterostructure films are fabricated through polystyrene spheres hetero-opal template using the convective self-assembly method to examine their potential for color purification. Their optical properties and photoluminescence have been investigated and compared with individual single inverse opals and reference (SiO$_2$:Tb^{3+} powder). The heterostructures are shown to possess two broad photonic stop bands separated by an effective pass band, causing suppression of blue, orange, and red emission bands corresponding to $^5D_4 \rightarrow {}^7F_j$; j = 6, 4, 3 transitions, respectively and an enhancement of green emission (i.e., $^5D_4 \rightarrow {}^7F_5$). Although the suppression of various emission occurs because of its overlap with the photonic band gaps (PSBs), the enhancement of green radiation is observed because of its location matching with the pass band region. The Commission International de l'Eclairage (CIE) chromaticity coordinates of the emission spectrum of the heterostructure based on polystyrene sphere of 390 and 500 nm diameter are x = 0.2936, y = 0.6512 and lie closest to those of standard green color (wavelength 545 nm). In addition, a significant increase observed in luminescence lifetime for $^5D_4$ level of terbium in inverse opal heterostructures vis-à-vis reference (SiO$_2$:Tb^{3+} powder) is attributed to the change in the effective refractive index.

KEYWORDS: *photonic crystal, heterostructure, inverse opal, lanthanides, spontaneous emission, color*
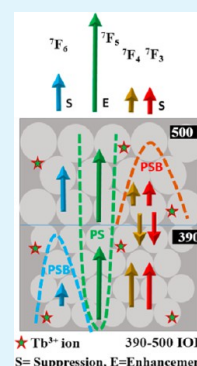
1. INTRODUCTION

Photonic crystals (PhCs) have attracted attention over the past decade because of their potential applications in waveguides, single-photon generation, low-threshold lasers, solar cells, photoelectrochemical water splitting, chemical and biosensors, etc.[1−7] Basically, their refractive index as well as dielectric constant vary periodically with spacing in the range of optical wavelengths. As a result, a forbidden/stop band is formed that prohibits certain light frequencies to pass through.[3,8] This feature can be exploited to control the spontaneous emission of an embedded light emitter in PhCs by manipulating the local photonic density of state. Several studies have been undertaken on the nature of spontaneous emission of semiconductor quantum dots,[9−11] organic dyes,[12−14] and rare-earth ions[15−20] containing PhCs. In recent years, immense interest has arisen in (i) complex PhCs, produced by introduction of crystal defects (such as point,[8,21,22] line,[23−25] or planar[26,27]) and (ii) photonic crystal heterostructures[28−30] (termed as PhCHs) because of their potential in improving ultrahigh quality nanocavity and light-harvesting efficiency besides developing quality optical filters.[31−34] A PhCH comprises two or more photonic crystals of different lattice parameters and/or refractive index materials and characterized by two or more photonic stop bands (PSBs).[29] Furthermore, a pass band (PB) can exist in between the PSBs of adjoining PhCs.[33] The combination of PB and PSBs may tune the spontaneous emission of embedded emitter (e.g., lanthanide ions/dyes/quantum dots) at different wavelengths.[35−37]

PhCHs can be fabricated as opal heterostructures (OH) and inverse opal heterostructures (IOH) but the later ones have certain advantages, e.g., wide photonic stop band, significant difference in refractive index, possibility of stop bands in all directions with a high refractive index matrix, and uniform distribution of infiltrated emitter species.[38,39] Nevertheless, opal heterostructures have been fabricated with embedded dye or CdTe crystals to study spontaneous emission characteristics.[35,40] For example, Beart et al.[35] have observed emission enhancement in pass band and suppression at stop bands region in a fluorophore (disodium fluorescein molecules) infiltrated opal heterostructure of silica spheres. Similarly, Gaponik et al.[40] found nonlinearity in emission in pass band region from CdTe nanocrystals when placed in a silica sphere-based opal heterostructure.

A few reports available on the fabrication of inverse opal heterostructures include sequential vertical deposition,[28] convective self-assembly,[41] and layer transfer approach method.[42] But, the investigations were focused only in describing techniques for preparation of the IOHs without embedding the luminescent species. Obviously, the emission characteristics could not be studied in them. Therefore, the current focus is to report the tuning of spontaneous emission from embedded lanthanide ions in inverse opal heterostructures fabricated by an established convective self-assembly method.[41] Lanthanide ions exhibit unique properties such as sharp emission, large Stokes shift, high resistance to optical blinking, and photobleaching
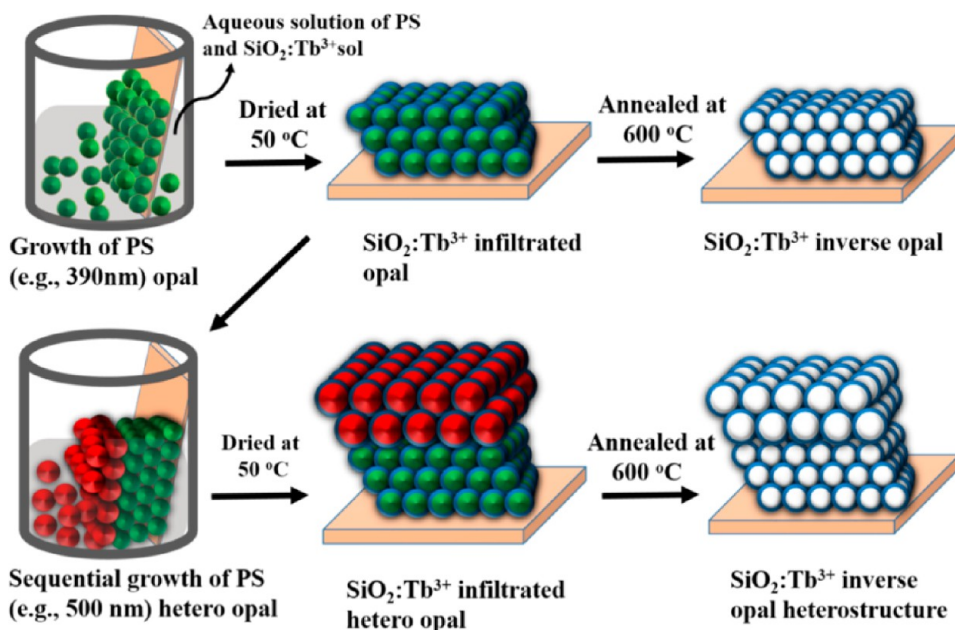
Figure 1. Schematic diagram for fabrication of SiO_2:Tb^{3+} single and hetero inverse opal structures (PS denotes polystyrene spheres).
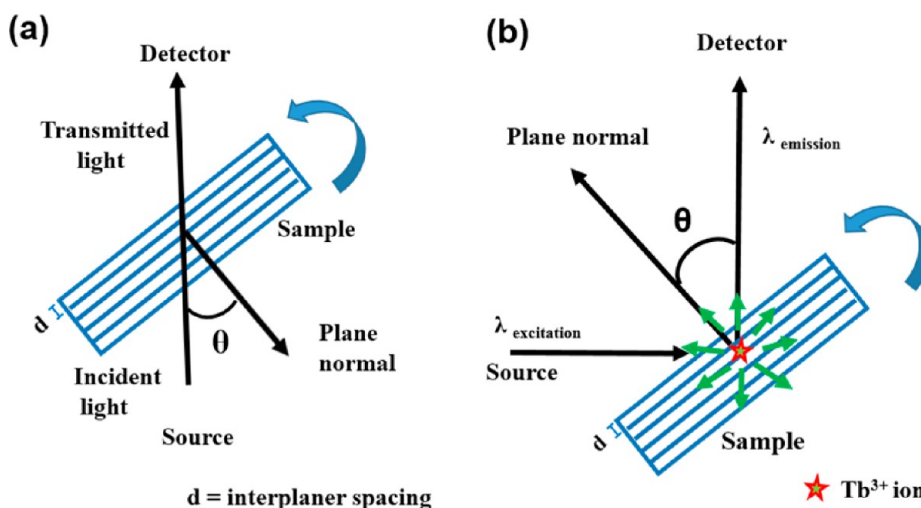

Figure 2. Arrangements for angle-dependent measurements: (a) transmittance spectrum and (b) photoluminescence from SiO_2:Tb^{3+} inverse opal structures.

besides distinctive ability of up-conversion and down-conversion.[43] As a consequence, they have found applications in light emitting diodes (LEDs),[44] security printing,[45] solid state displays,[46] lasers,[47] solar light harvesting,[48] biolabels,[49] optical data storage,[50] and bioimaging.[51] Emission from lanthanide ions arises due to inner shell 4f −4f transitions (being electric dipole in nature but induced by crystal field effects) in narrow bands and distinct long lifetime. Since the emission bandwidth of lanthanide ions is usually narrow, its complete suppression can occur if lies within the stop band region of PhC. The investigations undertaken earlier focused on the modification of lanthanide ions emission with PhCs possessing a single PSB.[15,19,52,53] Note that lanthanide ions exhibit several emissions (e.g., 488, 545, 580, and 625 nm for Tb^{3+} species) and hence a single PSB cannot possibly suppress (i) bands existing on both sides of a desired emission (545 nm) and/or (ii) two or more distant bands simultaneously.[52,54,55] The present work addresses this issue and deals with the spontaneous emission aspect of Tb^{3+} ion

embedded in silica IOH, exhibiting two PSBs with one PB in between, vis-à-vis IOs using SiO_2:Tb^{3+} powder as reference. It is demonstrated that the heterostructure suppresses the undesired emissions but improves the green band and so can serve as a color purifier. Further, the modified emissions have been examined in terms of their CIE coordinates and lifetime of $^5D_4$ state of terbium ions to understand the changes induced by the local environment.

2. EXPERIMENTAL SECTION

2.1. Preparation of Tb^{3+} Silica sol. Five milligrams of terbium nitrate hexahydrate ($Tb(NO_3)_3$.$6H_2O$, Aldrich, 99%) was first dissolved in 0.75 mL of distilled water and mixed with 1.5 mL of tetraethylorthosilicate (TEOS, Aldrich, 98%) and 3.9 mL of ethanol (Merck).The pH of the mixture was adjusted to 0.5−0.7 by adding few drops of HCl (35 wt %, Merck) and the mixture was continuously stirred at room temperature for 24 h to obtain a clear Tb^{3+}embedded silica sol.

2.2. Fabrication of SiO_2:Tb^{3+} Inverse Opal Structures. SiO_2:Tb^{3+} inverse opal single film- and double film heterostructure

inverse opals were fabricated by convective self-assembly method after optimization.[41] The process is depicted schematically in Figure 1 and involved three steps:

1. Preparation of SiO2:Tb³⁺ Infiltrated Opal Film of Polystyrene Spheres (PS). For this, a clean quartz substrate (size 5 mm × 10 mm × 2 mm) was treated with piranha solution (H_2SO_4/H_2O_2 = 3:1 v/v) at 80 °C for 2 h, washed with distilled water and dried. The substrate was then placed vertically in a beaker, containing the mixture of 80 μL of aqueous PS (390 nm) solution (10% by volume, procured from Bangs Laboratories, Fishers, USA), 8 μL of terbium-embedded silica sol and 2 mL of distilled water, and held at 50 °C for 12 h to form a silica-infiltrated PS opal film of 390 nm diameter. The opal films of other polystyrene spheres (500 or 280 nm diameter) were prepared in the same manner individually with a mixture of 60 μL (or 100 μL) of an aqueous solution (10% V) of 500 nm (or 280 nm) PS, 6 μL (or 8 μL) of terbium-embedded silica sol, and 2 mL of distilled water in each case and drying at 50 °C for 12 h.

(2). Fabrication of Heterostructure Opal. SiO2:Tb³⁺-infiltrated opal films of 390 and 500 nm polystyrene spheres were subsequently grown similarly over 280 and 390 nm opal films, respectively, and held again at 50 °C for 12 h to obtain silica-infiltrated heterostructures.

(3). Development of Inverse Opal Heterostructure. SiO2:Tb³⁺-infiltrated opal films with 280, 390, and 500 nm diameter PS individually and 280−390 and 390−500 nm heterostructure were heated at 600 °C for 3 h to remove the polystyrene. This process yielded a set of five samples of single- as well as hetero- inverse opal structure of air spheres (termed as 280 IO, 390 IO, 500 IO, 280−390 IOH, and 390−500 IOH).

2.3. Characterization Techniques. Microstructure of each sample was observed in a field emission scanning electron microscope (Carl Zeiss NTS GmbH-SUPRA 40VP). Although a Varian Cary 5000 UV−vis−NIR spectrophotometer was employed for measuring the optical reflectance, Hitachi model U-3310 double beam UV−visible spectrophotometer was engaged to record the transmittance spectra. Further, the photoluminescence (PL) and fluorescence lifetime data were collected with a fluorimeter (Edinburgh instrument model FLS 920) using Xenon flash lamp (Xe900, 450 W) and micro flash lamp (μF920, 60W), respectively. For obtaining the angular-dependent optical transmission, PL, and lifetime data, we mounted the sample on a goniometer head and rotated it manually to adjust the incident angle. The arrangements used are shown schematically in Figure 2.

3. RESULTS AND DISCUSSION

Figure 3a−c shows the FESEM images of 280 IO, 390 IO, and 500 IO inverse opal structures. The ordered close packing of air spheres is noticed in each case with hexagonal configuration (i.e., coordination six) and separation of 200, 273, and 358 nm, respectively. The stacking of close-packed layers of hard spheres is known to generate ordered (cubic, hexagonal, or both mixed) structures with identical filling factors of ∼74%. On the basis of evidence gathered through microscopic examination and thermodynamic calculations, the cubic-close packed (c.c.p.) structure is considered to be most stable.[56,57] The distance between the hard spheres in close packing should therefore be just equal to their diameter. However, the above results invariably show smaller distance than the diameter of the original polystyrene spheres, e.g., the separation observed are 200, 273, and 358 nm against sphere diameters of 280, 390, and 500 nm, respectively. Obviously, there is shrinkage of ∼28−30% caused perhaps by decomposition and removal of PS content and release of adsorbed water from silica. The micrographs presented in Figure 3a−c show air spheres as gray and regions containing SiO2:Tb³⁺ as white and are similar to those reported in the literature for c.c.p. structures. Figure 4a, b and Figure S1−S3 (Supporting Information) depict cross-sectional images of 280−390 IOH and 390−500 IOH structures, respectively. The interface between the two types of inverse opal in each case is clearly visible.
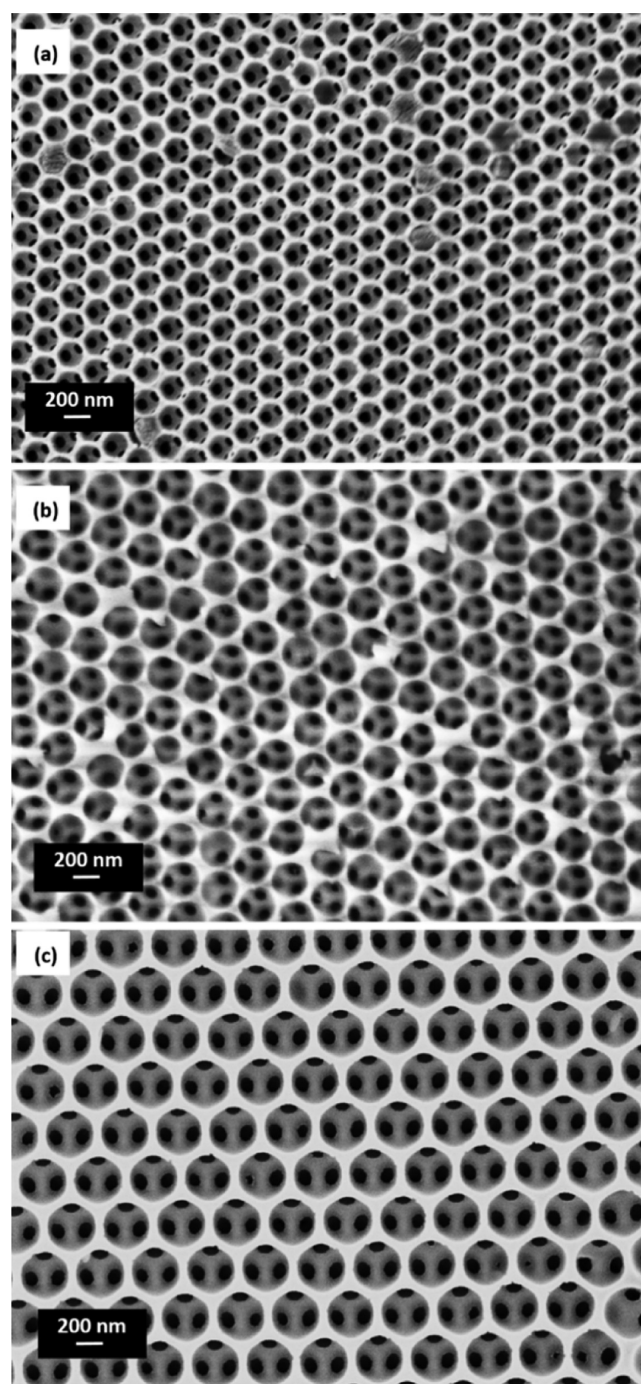

Figure 3. Field-emission scanning electron microscope (FESEM) images (top view) of single inverse opal structures: (a) 280 IO, (b) 390 IO, and (c) 500 IO.

The digital optical photograph of 280−390 IOH, 390−500 IOH, 280 IO, 390 IO and 500 IO shown in Figure 5a−e reveals different colors (e.g., cyan/blue, cyan/red, blue, cyan, and red, respectively) because of variation in their reflection behavior. The color mixing at some places may arise because of orientation difference of domains and/or peeling off effects in inverse opal structures. It is evident that the method used gives good- quality inverse opals with reasonable ordering extending to several micrometers.

Figure 6a−c shows optical transmittance and diffuse reflectance spectra of (280 IO, 390 IO, and 500 IO), 280−390
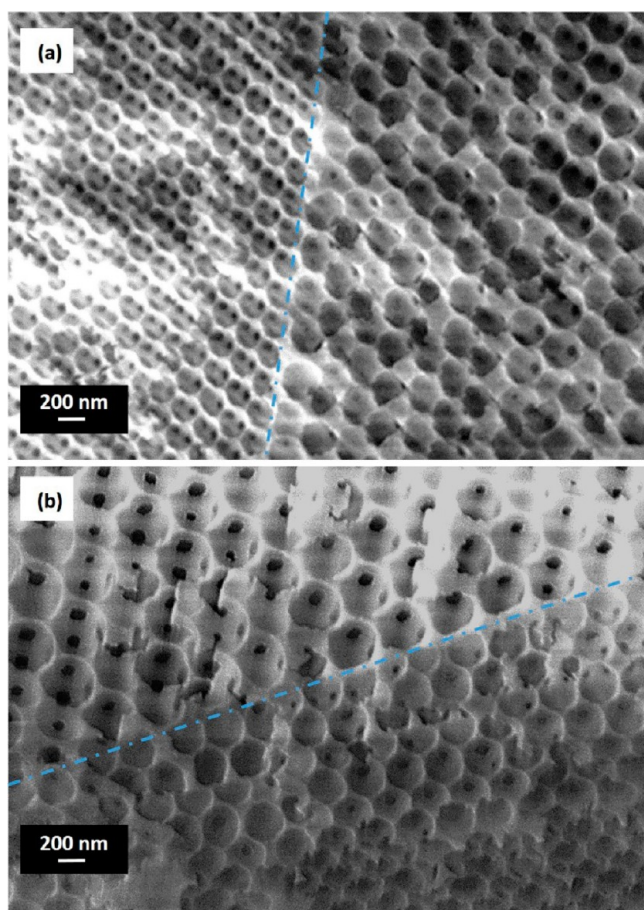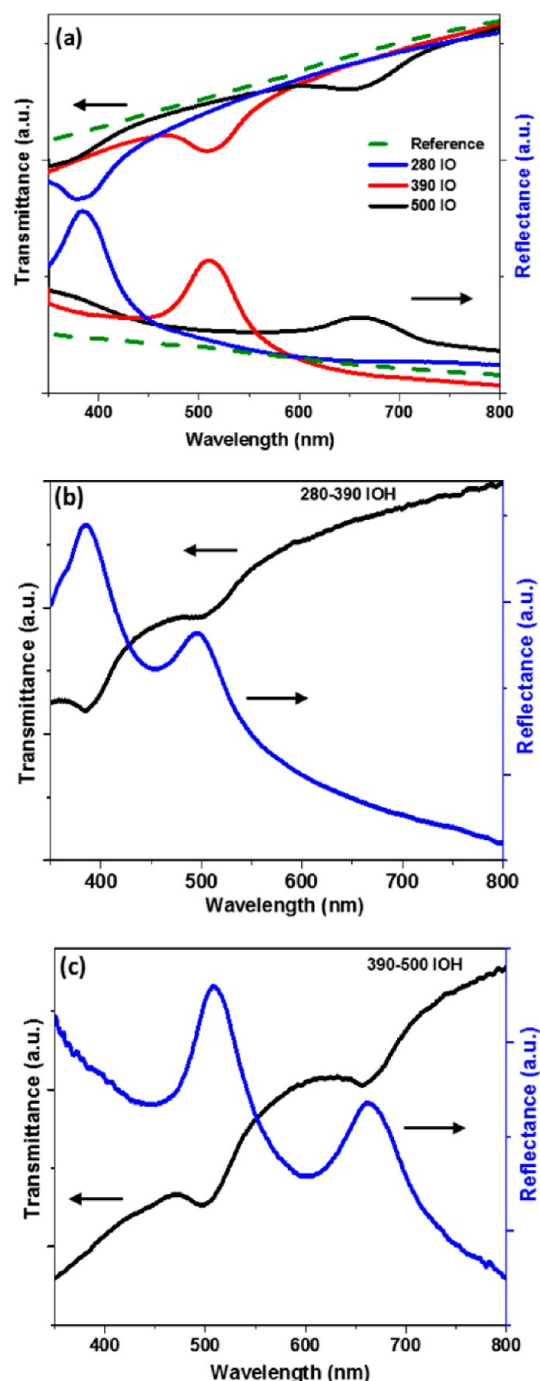
Figure 4. Field-emission scanning electron microscope (FESEM) images (cross-sectional) of inverse opal heterostructures: (a) 280−390 IOH and (b) 390−500 IOH. The blue dashed line indicates the interface in inverse opal heterostructures.
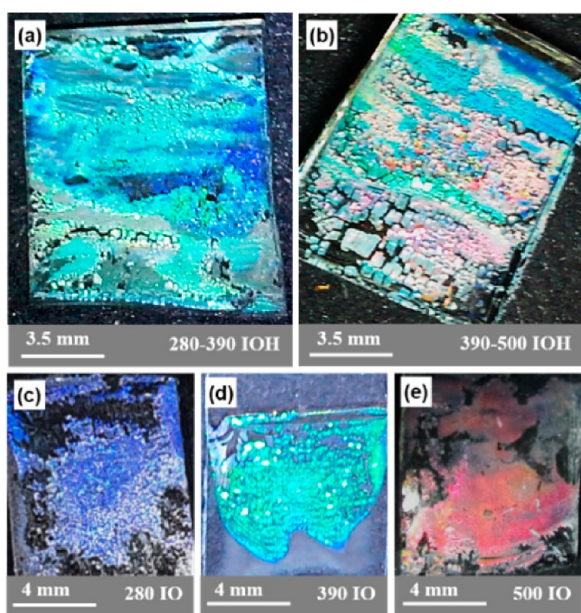
Figure 5. Digital optical photographs of (a) 280−390 IOH, (b) 390−500 IOH, (c) 280 IO, (d) 390 IO, and (e) 500 IO structures.


Figure 6. Optical transmittance (left) and diffuse reflectance (right) spectra of (a) 280 IO, 390 IO, 500 IO and reference, (b) 280−390 IOH, and (c) 390−500 IOH samples; Measurements undertaken at the normal incidence ($\theta = 0°$).

reflectance spectra represent the PSB position at 380, 505, and 660 nm for the 280 IO, 390 IO, and 500 IO, respectively. Notice that in case of 280−390 IOH and 390−500 IOH, there are two PSB positions in each, close to those found in the individual inverse opals and displayed in Figure 6a. The nature of peak of IOH in general depends on several factors, i.e., sample thickness, interface effects, light incident side, scattering, wavelength-dependent variation of reflectance, etc.[33,58−60] In addition, valleys visible at ∼450 and ∼595 nm in reflectance spectra (Figure 6b, c) represent the pass bands of 280−390 IOH and 390−500 IOH, respectively.

IOH and 390−500 IOH at normal incident of light. The minimum in the transmittance and corresponding peak in

Figure 7a,b shows the angle-dependent transmittance spectra of 280−390 IOH and 390−500 IOH measured when the
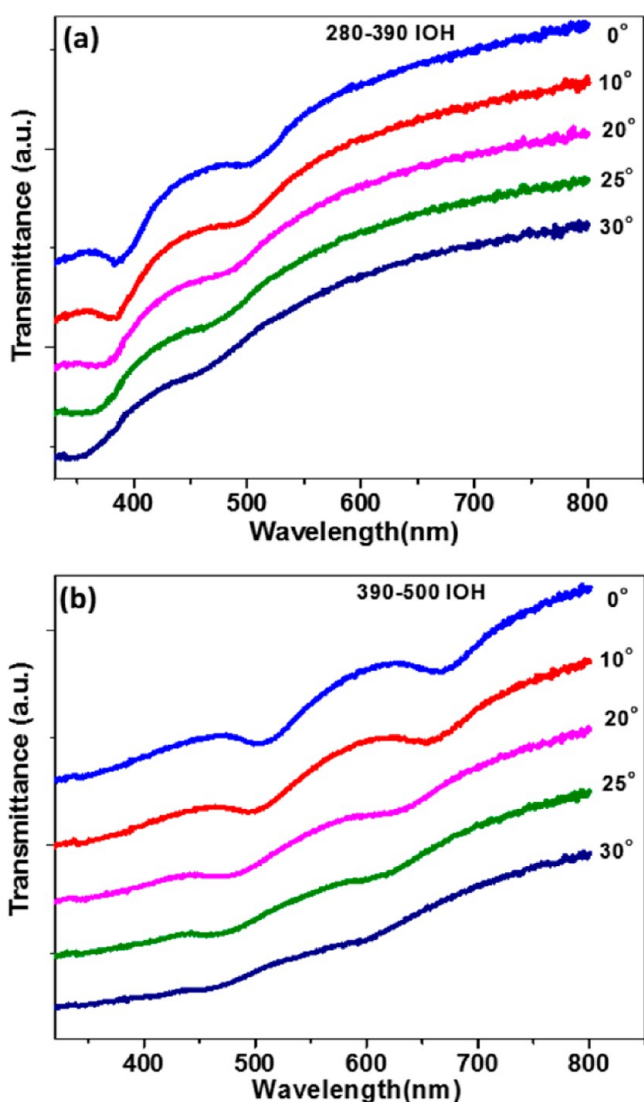

Figure 7. Angle-dependent transmittance spectra inverse opal heterostructures: (a) 280−390 IOH and (b) 390−500 IOH.

incident beam makes an angle (θ = 0, 5, 10, 20, 25, and 30°) with the sample normal. These indicate shift in PSB toward a shorter wavelength with increase in the incident angle (θ). By taking refraction into consideration the modified Bragg's law governing the interference phenomenon is written as[61]

$$2d\sqrt{n_{eff}^2 - \sin^2\theta} = n\lambda \quad (1)$$

where d is the spacing between close-packed planes, θ is the angle between the incident light and normal to the sample plane, n_{eff} is the effective refractive index, n is the order of diffraction, and λ is the wavelength of incident radiation (or just the PSB position in the transmission spectrum). For the first order diffraction, $n = 1$ and so λ should decrease with increase in "θ" for a particular d. This is indeed observed above in Figure 7a, b and Figure S4 (Supporting Information). The two PSB positions observed in each heterostructure correspond to spheres of different size present in top and bottom portion of the inverse opals. According to the eq 1, for $n = 1$, λ^2 versus $\sin^2\theta$ plot should

be a straight line with slope giving d and the intercept on the y-axis determining n_{eff}. Figure 8a,b indeed depicts straight lines with respective d and n_{eff} values as deduced specified therein.
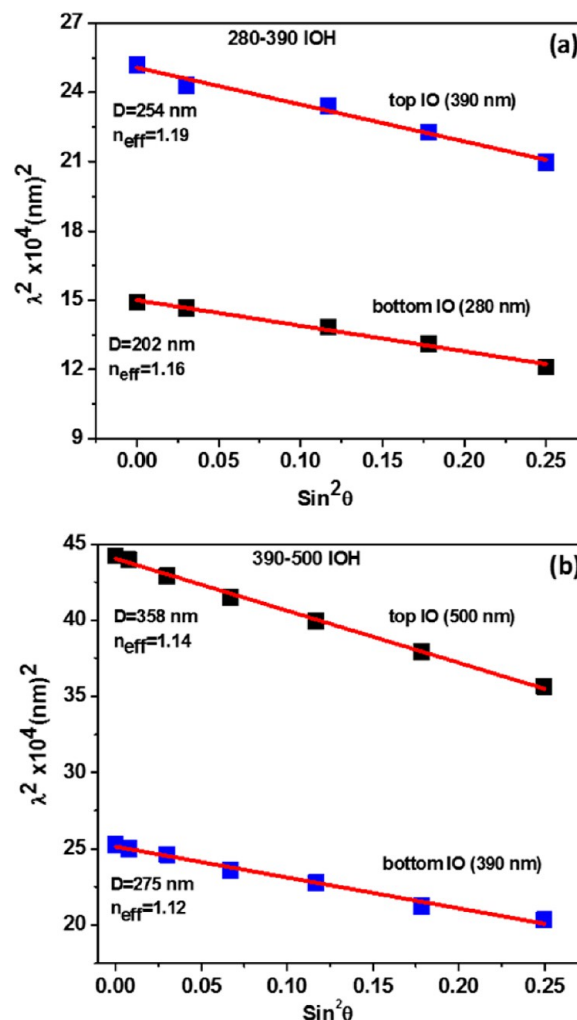
Figure 8. λ^2 versus $\sin^2\theta$ plots for inverse opal layers in (a) 280−3900 IOH and (b) 390−500 IOH showing straight lines allowing deduction of d and, in turn, D ($=\sqrt{(3/2)d}$) from the slope and n_{eff} using intersection at ordinate.

The effective refractive index (n_{eff}) for an inverse opal structure is defined as

$$n_{eff} = n_{SiO_2}\phi + n_{air}(1 - \phi) \quad (2)$$

where n_{SiO2} = 1.455 and n_{air} = 1 are the refractive indices of silica and air, respectively and ϕ is the packing fraction of silica in the inverse opal. For an ideal close-packed structure n_{eff} turns out to be 1.12 as ϕ = 0.26. Notice that the values of n_{eff} obtained from experimental data lie in the range of 1.12−1.18. The variation in n_{eff} can be attributed to nonideal packing with slightly larger filling factor (ϕ) of SiO$_2$. The interplanar spacing d is related to the sphere diameter in a close-packed structure or air sphere separation (D) in an inverse opal structure as $d = (2/3)^{1/2}D$. Thus, D values can be determined using d obtained from the λ^2 versus $\sin^2\theta$ plots (Figure 8a, b) and measured from FESEM images (Figures 1 and 2) as well. The results are summarized in Table 1 and reveal good correspondence in D values.

Table 1. Comparison of Pore Diameter (D) Observed from FESEM and Optical Properties: Photonic Stop Band (PSB), Interplanar Spacing (d_{111}), Air Sphere Diameter ($D_{optical}$, D_{SEM}), and Percentage Shrinkage of PS Diameter of Various Inverse Opal (IO) and Inverse Opal Hetero (IOH) Structures

| sample	PSB position (nm)	d_{111} (nm)	$D_{optical} = \sqrt{(3/2)}d_{111}$ (nm)	D_{SEM} (nm)	shrinkage (%)
280−390 IOH:					
280 bottom layer	384	166	204	209	24.5
390 top layer	500	215	263	268	31.2
390−500 IOH:					
390 bottom layer	502	224	274	278	28.8
500 top layer	664	292	357	362	27.6
280 IO	380			200	28.6
390 IO	505			273	29.9
500 IO	660			358	28.4

Table 2. Relative Integrated Intensity of Various Emissions from the Infiltrated $SiO_2:Tb^{3+}$ Ions in Various Inverse Opal (IO) and Inverse Opal Hetero (IOH) Structures

| samples	relative intensity of Tb^{3+} ion emission corresponding to $^5D_4 \rightarrow ^7F_i$ (j = 6, 5, 4, 3) transitions			
	$^5D_4\rightarrow^7F_6$ (486 nm)	$^5D_4\rightarrow^7F_5$ (545 nm)	$^5D_4\rightarrow^7F_4$ (584 nm)	$^5D_4\rightarrow^7F_3$ (620 nm)
reference sample	19.4	61.5	10.3	8.8
390−500 IOH	18.1	69.0	7.1	4.8
280−390 IOH	16.2	62.3	10.8	9.6
500 IO	24.8	62.5	7.6	5.0
390 IO	12.4	61.8	12.2	13.5
280 IO	19.8	62.0	9.9	8.3

Figure 9a−e depicts the photoluminescence spectra of 280 IO, 390 IO, 500 IO, 280−390 IOH, and 390−500 IOH along with that of reference ($SiO_2:Tb^{3+}$ gel powder) in each as recorded with a detector held at 20° from the sample normal (Figure 2b). The 390−500 IOH shows different colors (Figure 5b) in various parts, indicating nonuniformity of the heterostructure. This is happening because of peeling of the top layer at some places during the processing steps. Nevertheless, photoluminescence measurements have been made carefully by focusing the light on the portion of heterostructure only. All these show four sharp emission bands at 486, 545, 584, and 620 nm corresponding to $^5D_4 \rightarrow ^7F_j$ (j = 6, 5, 4, 3) transitions of Tb^{3+} species, respectively (Table 2). To visualize the relative change in the emission,

background correction is made in each spectrum and normalization undertaken with the total intensity. Whereas the blue emission band at 486 nm is reduced in 390 IO (Figure 9b), the yellow and red emission peaks at 584 and 620 nm, respectively, get suppressed in 500 IO with respect to the reference; the reason being overlap of emission band(s) with the PSB of respective inverse opal structures. Further, enhancement of emission peak is observed at 584 and 620 nm in 390 IO and at 486 nm in 500 IO vis-a-vis reference (Figure 9b, c). In the case of 390−500 IOH (Figure 9e), the two PSBs of the heterostructure overlap with the above three emission bands at 486, 584, and 620 nm simultaneously. The overall effect is that the emission peaks are suppressed reasonably at 584 and 620 nm and marginally at 486 nm. The functions of top layer are (i) suppression of both 584 and 620 nm emissions because of its broad PSB and (ii) reflection of these very emissions from Tb^{3+} ions present in the bottom layer. On the other hand, top and bottom inverse opals induce opposite changes (i.e., enhancement and suppression, respectively) in the 486 nm emission and leads eventually to
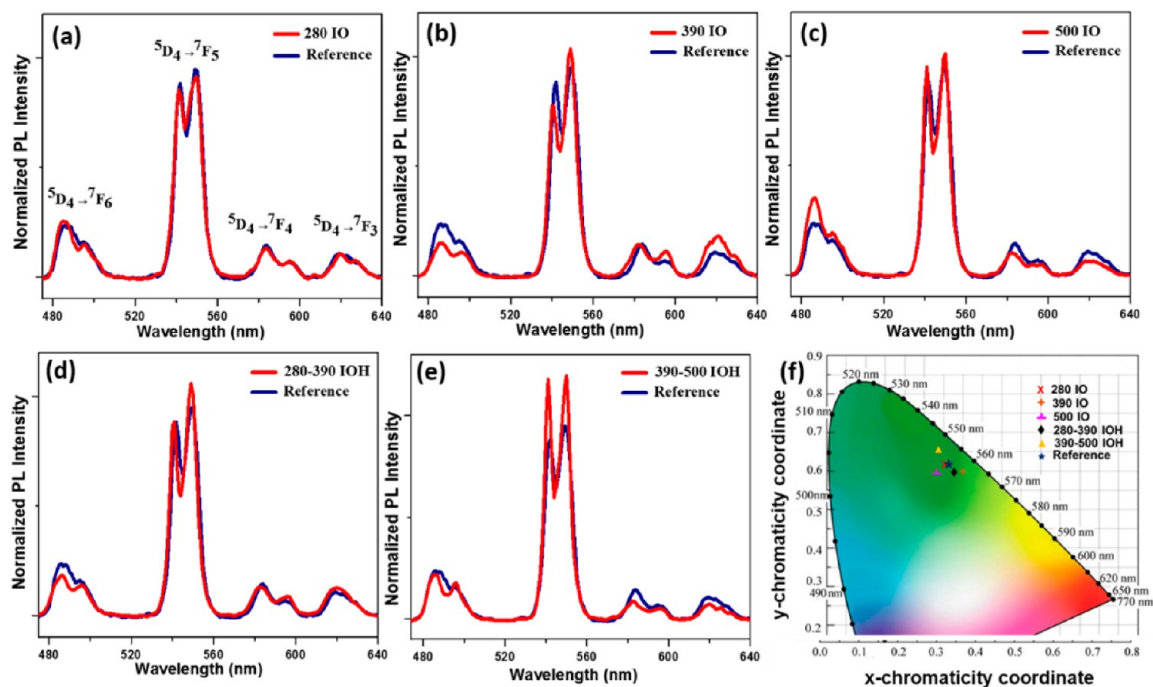
Figure 9. Photoluminescence spectra of $SiO_2:Tb^{3+}$ inverse opal structures along with reference: (a) 280 IO, (b) 390 IO, (c) 500 IO, (d) 280−390 IOH, and (e) 390−500 IOH samples; and (f) CIE coordinates of Tb^{3+} emission in all the sample. Excitation wavelength 230 nm, emission spectra measured at θ = 20° (Figure 2b).

somewhat less suppression vis-à-vis reference. The marked enhancement of Tb^{3+} green emission at 545 nm is arising due to matching with the pass band of the inverse opal heterostructure itself (Table 2). Figure 10 depicts the modifications in Tb^{3+} ion emission in 390−500 IOH vis-à-vis reference induced by PSB and PB effects schematically.
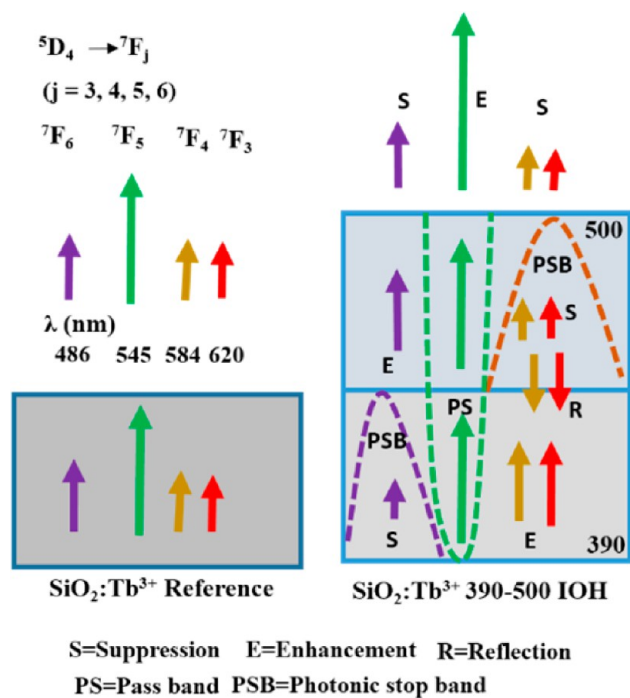
Figure 10. Schematic representation of Tb^{3+} ion emission modifications in 390−500 IOH inverse opal heterostructure vis-à-vis reference induced by PSB and PB effects at $\theta = 20°$.

The suppression of emission in IOHs and IOs can be understood by confinement of photon within PhCs due to Bragg diffraction.[62] Alternatively, it amounts to reduction in the number of optical modes available for photon propagation at frequencies lying within the PSB.[63] The enhancement of emission is linked to local density of states (or the number of available optical modes) determined by the environment around the emitter. Because the total number of states is conserved, their redistribution leads to suppression within and enhancement outside the PSB in PhCs. Thus, an increase in local density of states will speed up the emission process and shows enhancement.[64] In other words, because the rate of relaxation through one of the transition is reduced due to energy overlap with the PSB, the electrons prefer other transition(s) existing outside the stop band. Since the pass band region lies in between PSBs in inverse opal heterostructure local density of states is expected to be high leading to enhancement in the emission withinin that range. Gaponik et al.[40] have studied the luminescent characteristics of opal heterostructure by incorporating CdTe nanocrystals in the bottom layer only. Accordingly, the passband between the two PSBs causes nonlinearity with no enhancement in emission due to interface effects. On the other hand, Baert et al.[35] introduced dye in both top and bottom layers of the hetero-opal and found emission enhancement in pass band region and suppression on its right side. The present finding in Tb^{3+}-embedded 390−500 IOH is consistent with that of Baert et al.[35] and amounts to green color purification vis-à-vis single inverse

opal and reference sample. The study related to 390−500 IOH with Tb^{3+} in the bottom layer alone is under progress and expected to reveal the role of the top layer as well as the emitter in understanding the observed enhancement of green emission better.

To justify the occurrence of the above emission modifications (suppression as well as enhancement) in 390−500 IOH because of two PSBs and a passband, the nature of 280−390 IOH has also been investigated. Figure 9d depicts the emission spectra of 280−390 IOH with PSBs at ~377 and ~484 nm and a pass band at 430 nm. In 280−390 IOH, photonic stop band at 484 nm overlaps with blue emission (486 nm) and causes suppression. On the other hand, the PSB at 377 nm lies outside the range of Tb^{3+} emission and hence shows no effect. To reveal the respective changes in the terbium green emission, the CIE chromaticity coordinates of all the inverse opal samples have been deduced and presented in Figure 9f. Notice that the CIE chromaticity coordinates of 390−500 IOH are much closer to those of CIE1931 green color ($x = 0.2738, y = 0.7174$)[65] in comparison to 280 IO, 390 IO, 500 IO, 280−390 IOH, and SiO_2:Tb^{3+} gel power (See Table 3). Figure 11 shows the angle-dependent emission

Table 3. CIE Coordinate of 280IO, 390 IO, 500 IO, 280−390 HIO 390−500 HIO, and Reference Silica Samples; CIE Coordinates Are Compared with CIE (1931) Green Coordinate

	CIE chromaticity coordinate	
sample	x	y
green (CIE1931) [65]	0.2738	0.7174
reference sample	0.3214	0.6146
390−500IOH	0.2936	0.6512
280−390 IOH	0.3301	0.6023
500 IO	0.2975	0.6059
390 IO	0.3512	0.6025
280IO	0.3150	0.6134

spectra of 390−500 IOH in the range $\theta = 20−50°$. It reveals the suppression of 545 nm green emission at $\theta = 40°$ because of the overlap with the PSB of the top inverse opal layer. Also, 486 nm blue emission is enhanced as it lies within the pass band region. With further increase in θ to 50°, PSB of the top layer shifts
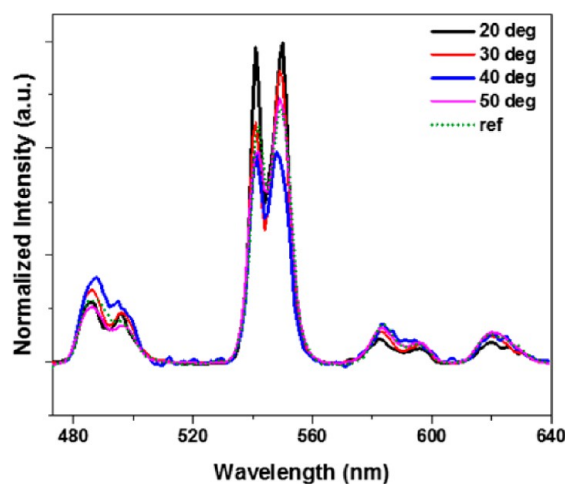
Figure 11. Angle-dependent photoluminescence spectra of Tb^{3+} in 390−500 IOH. Excitation wavelength 230 nm.

toward a lower wavelength, and so the suppression of 545 nm green emission ceases.

To understand the nature of total SER in $^5D_4$ excited state, the lifetime measurements have been made as described in Section 2.3 for all the samples. Figure 12a shows the decay curves in 280
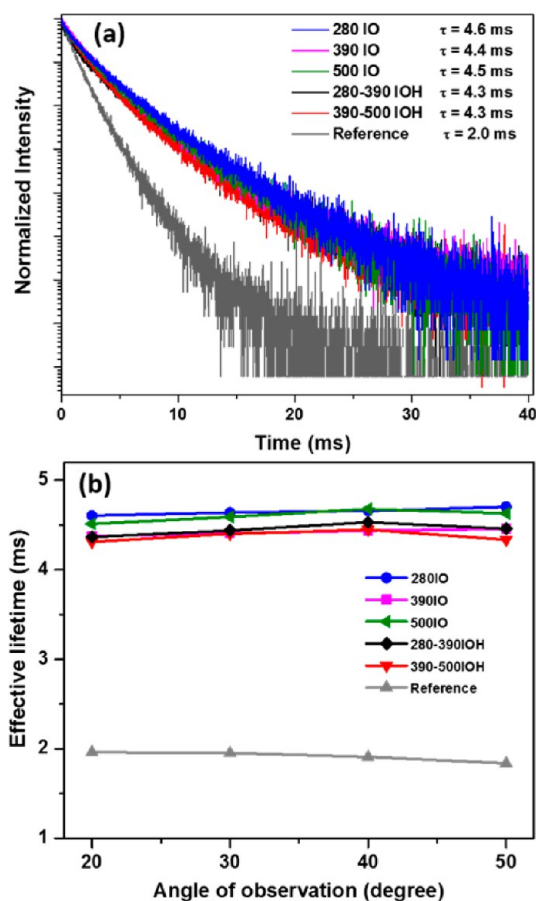
Figure 12. (a) Photoluminescence decay curves of 545 nm emission corresponding to $^5D_4 \rightarrow {}^7F_5$ transition of Tb^{3+} ions from 280 IO, 390 IO, 500 IO, 280−390 IOH, 390−500 IOH, and reference. Excitation wavelength 230 nm, emission spectra measured at $\theta = 20°$ (Figure 2b). (b) Effective luminescence lifetime for 545 nm emission of Tb^{3+} ion at various observation angles in 280 IO, 390 IO, 500 IO, 280−390 IOH, 390−500 IOH, and reference.

IO, 390 IO, 500 IO, 280−390 IOH, 390−500 IOH, and the reference, obtained with a detector held at 20° from the sample normal. These are fitted using the expression

$$I(t) = A + \sum_i B_i e^{-t/\tau_i} \tag{3}$$

where τ_i ($i = 1, 2, 3\cdots$) is the characteristic lifetime, B_i is the preexponential factor called weighted amplitude, and A is an additional parameter. The chi square (χ^2) of different fittings is found to lie in the range 1.6−1.9. The average luminescence lifetime has been deduced from the relation[66]

$$\tau = \frac{B_1\tau_1^2 + B_2\tau_2^2 + B_3\tau_3^2}{B_1\tau_1 + B_2\tau_2 + B_3\tau_3} \tag{4}$$

The deduced values of τ are ∼4.6, 4.4, 4.5, 4.3, 4.3, and 2 ms for 280 IO, 390 IO, 500 IO, 280−390 IOH, 390−500 IOH, and reference, respectively (Figure 12a). The sensitivity of the lifetime measurement is high and lies in the microsecond range.

Further, the standard deviation in lifetime values has been around ±0.15 ms. That means, the lifetime difference in various samples appears to be real and possibly arising due to minor variation in the filling fraction of silica (i.e., changes in effective refractive index) considering the low lifetime value displayed by the reference and the discussion that follows now. Obviously, the lifetime (τ) increased to (2−2.3) times in all the inverse opal structures vis-à-vis the reference. Such an increase in luminescence lifetime is observed earlier too in lanthanide ions embedded inverse opals and attributed to either variation in the refractive index[15,53,67] or PSB effect.[19,63,68] However, the lifetime data of various single- and hetero- inverse opals presented above reveal enhancement to almost the same level despite of noticeable differences in the PSB position. Hence, the origin of enhanced lifetime observed here for Tb^{3+} green emission lies with refractive index itself and not the PSB effect. The luminesce lifetime (τ) of lanthanide ions present in a medium is related to the effective refractive index as[69]

$$\tau \approx \frac{\lambda_0^2}{f(ed)\left[\frac{1}{3}(n_{eff}^2 + 2)\right]^2 n_{eff}} \tag{5}$$

where λ_0 is the wavelength of light in vacuum and f (ed) is oscillator strength of electric dipole transition, and n_{eff} is the effective refractive index of the material, given by eq 2. Note that the values of refractive index of all IO and IOH samples are ∼1.13 (much smaller than 1.455 of the reference) because silica- to air-volume fraction remains nearly the same. As a consequence, eq 5 gives luminescence lifetime of Tb^{3+} ions in IO and IOH as about 2-times of the reference, if f (ed) is considered as constant, and close to the experimental values.

Figure 12b shows the lifetime data of Tb^{3+} green light emitted at 545 nm as a function of angle (θ), the detector is making with the sample normal (Figure 2b). It is interesting that the lifetime of various IO and IOH samples remain essentially the same at different angle (θ), lie within in the standard deviation. The present finding is consistent with the report of Wang et al.,[15] who studied the luminescent dynamics and angle-resolved emission spectra of Eu^{3+} ion containing poly methyl methacrylate (PMMA) opal photonic crystals and simulated the total density of states (DOS) numerically. Accordingly, in low dielectric PhC, the total density of states remain essentially the same despite of distinguished angular distribution of local density of states. As a consequence, the total emission spontaneous rate (SER) of all the Eu^{3+} $^5D_0−{}^7F_J$ transitions taken together turns out to be constant and independent of PSB position. Further, SER value is determined by the effective refractive index of the photonic crystal itself. But, SER of a specific transition (e.g., $^5D_0−{}^7F_2$) is spatially distributed, suppressed or enhanced in certain directions depending on the increase or reduce of the optical modes. Thus, the luminescence lifetime provides information about all the $^5D_0−{}^7F_J$ transitions rather than that of any specific one because of the excited state being $^5D_0$ itself for them all.

In the present case, the total SER of $^5D_4−{}^7F_J$ transitions of Tb^{3+} ion is conserved and no change occurs with the angle (θ). As a consequence, the luminescent lifetime of $^5D_4$ excited state of SiO_2:Tb^{3+} IO and IOH samples remains the same at all angles (θ) with no bearing on the local density of states. The reason being the correspondence of luminescent lifetime with the total SER ($\sum {}^5D_4-{}^7F_J$) of all transitions and not with any individual one. In fact, all the emissions are occurring from $^5D_4$ level of Tb^{3+} ions.

4. CONCLUSIONS

Tb^{3+} embedded silica inverse opal heterostructures (IOHs) can be fabricated successfully using an improved convective self-assembly method via polystyrene spheres (diameter 280, 390, and 500 nm) hetero-opal template in $SiO_2:Tb^{3+}$ matrix. The two photonic stop bands appearing at 484 and 610 nm in 390−500 IOH cause suppression of Tb^{3+} ion blue, orange and red emission bands corresponding to $^5D_4 \rightarrow {}^7F_j$; $j = 6, 4, 3$ transitions. The enhancement of green emission band at ∼545 nm results because of the pass band effect. The CIE chromaticity coordinates of modified emission of 390−500 IOH deduced as $x = 0.2936$, $y = 0.6512$ are closest to those of green color (545 nm). The lifetime values of Tb^{3+} ions emission at 545 nm in various inverse opal heterostructures are ∼2.4 time larger to that of reference sample. The marked improvement in lifetime is attributed to changes in effective refractive index. This correlation is corroborated by the angle dependence lifetime measurements data as well.

■ ASSOCIATED CONTENT

Ⓢ Supporting Information

FESEM images of Silica infiltrated PS hetero opal templates, inverse opal heterostructure (280−390 IOH and 390−500 IOH) at various magnifications, and plot of PSB position with incident angle. The Supporting Information is available free of charge on the ACS Publications website at DOI: 10.1021/acsami.5b01615.

■ AUTHOR INFORMATION

Corresponding Authors

*E-mail: srisiva@iitk.ac.in. Tel.: +91-512-2597697. Fax: +91-512-2597664.
*E-mail: jk@iitk.ac.in. Tel.: +91-512-2597107.

Notes

The authors declare no competing financial interest.

■ REFERENCES

(1) Lin, S.-Y.; Chow, E.; Hietala, V.; Villeneuve, P. R.; Joannopoulos, J. D. Experimental Demonstration of Guiding and Bending of Electromagnetic Waves in a Photonic Crystal. *Science* 1998, 282, 274−276.

(2) Santori, C.; Fattal, D.; Vuckovic, J.; Solomon, G. S.; Yamamoto, Y. Indistinguishable Photons from a Single-Photon Device. *Nature* 2002, 419, 594−597.

(3) Yablonovitch, E. Inhibited Spontaneous Emission in Solid-State Physics and Electronics. *Phys. Rev. Lett.* 1987, 58, 2059−2062.

(4) Guldin, S.; Hüttner, S.; Kolle, M.; Welland, M. E.; Müller-Buschbaum, P.; Friend, R. H.; Steiner, U.; Tétreault, N. Dye-Sensitized Solar Cell Based on a Three-Dimensional Photonic Crystal. *Nano Lett.* 2010, 10, 2303−2309.

(5) Zhang, Z.; Zhang, L.; Hedhili, M. N.; Zhang, H.; Wang, P. Plasmonic Gold Nanocrystals Coupled with Photonic Crystal Seamlessly on TiO2 Nanotube Photoelectrodes for Efficient Visible Light Photoelectrochemical Water Splitting. *Nano Lett.* 2012, 13, 14−20.

(6) Waterhouse, G. I. N.; Wahab, A. K.; Al-Oufi, M.; Jovic, V.; Anjum, D. H.; Sun-Waterhouse, D.; Llorca, J.; Idriss, H. Hydrogen production by Tuning the Photonic Band Gap with the Electronic Band Gap of TiO2. *Sci. Rep.* 2013, 3, 2849.

(7) Fenzl, C.; Hirsch, T.; Wolfbeis, O. S. Photonic Crystals for Chemical Sensing and Biosensing. *Angew. Chem., Int. Ed.* 2014, 53, 3318−3335.

(8) Joannopoulos, J. D.; Villeneuve, P. R.; Fan, S. Photonic Crystals: Putting a New Twist on Light. *Nature* 1997, 386, 143−149.

(9) Husken, B. H.; Koenderink, A. F.; Vos, W. L. Angular Redistribution of Near-Infrared Emission from Quantum Dots in Three-Dimensional Photonic Crystals. *J. Phys. Chem. C* 2012, 117, 3431−3439.

(10) Blanco, A.; López, C.; Mayoral, R.; Míguez, H.; Meseguer, F.; Mifsud, A.; Herrero, J. Cds Photoluminescence Inhibition by a Photonic Structure. *Appl. Phys. Lett.* 1998, 73, 1781−1783.

(11) Vion, C.; Barthou, C.; Bénalloul, P.; Schwob, C.; Coolen, L.; Gruzintev, A.; Emel'chenko, G.; Masalov, V.; Frigerio, J.-M.; Maître, A. Manipulating Emission of CdTeSe Nanocrystals Embedded in Three-Dimensional Photonic Crystals. *J. Appl. Phys.* 2009, 105, 113120.

(12) Kolaric, B.; Baert, K.; Van der Auweraer, M.; Vallée, R. A. L.; Clays, K. Controlling the Fluorescence Resonant Energy Transfer by Photonic Crystal Band Gap Engineering. *Chem. Mater.* 2007, 19, 5547−5552.

(13) Nair, R. V.; Tiwari, A. K.; Mujumdar, S.; Jagatap, B. N. Photonic-Band-Edge-Induced Lasing in Self-Assembled Dye-Activated Photonic Crystals. *Phys. Rev. A* 2012, 85, 023844.

(14) Romanov, S. G.; Maka, T.; Sotomayor Torres, C. M.; Müller, M.; Zentel, R. Photonic Band-Gap Effects upon the Light Emission From a Dye−Polymer−Opal Composite. *Appl. Phys. Lett.* 1999, 75, 1057−1059.

(15) Wang, W.; Song, H.; Bai, X.; Liu, Q.; Zhu, Y. Modified Spontaneous Emissions of Europium Complex in Weak PMMA Opals. *Phys. Chem. Chem. Phys.* 2011, 13, 18023−18030.

(16) Yang, Z.; Zhou, J.; Huang, X.; Yang, G.; Xie, Q.; Sun, L.; Li, B.; Li, L. Photonic Band Gap and Photoluminescence Properties of LaPO4:Tb Inverse Opal. *Chem. Phys. Lett.* 2008, 455, 55−58.

(17) Aloshyna, M.; Sivakumar, S.; Venkataramanan, M.; Brolo, A. G.; van Veggel, F. C. J. M. Significant Suppression of Spontaneous Emission in SiO2 Photonic Crystals Made with Tb3+-Doped LaF3 Nanoparticles. *J. Phys. Chem. C* 2007, 111, 4047−4051.

(18) Liao, J.; Yang, Z.; Lai, S.; Shao, B.; Li, J.; Qiu, J.; Song, Z.; Yang, Y. Up-conversion Emission Enhancement of NaYF4: Yb, Er Nanoparticles by Coupling Silver Nanoparticle Plasmons and Photonic Crystal Effects. *J. Phys. Chem. C* 2014, 118, 17992−17999.

(19) Qu, X.; Song, H.; Pan, G.; Bai, X.; Dong, B.; Zhao, H.; Dai, Q.; Zhang, H.; Qin, R.; Lu, S. Three-Dimensionally Ordered Macroporous ZrO2:Eu3+: Photonic Band Effect and Local Environments. *J. Phys. Chem. C* 2009, 113, 5906−5911.

(20) Kubrin, R.; do Rosario, J. J.; Lee, H. S.; Mohanty, S.; Subrahmanyam, R. P.; Smirnova, I.; Petrov, A.; Petrov, A. Y.; Eich, M.; Schneider, G. A. Vertical Convective Coassembly of Refractory YSZ Inverse Opals from Crystalline Nanoparticles. *ACS Appl. Mater. Interfaces* 2013, 5, 13146−13152.

(21) García, P. D.; Sapienza, R.; Toninelli, C.; López, C.; Wiersma, D. S. Photonic Crystals with Controlled Disorder. *Phys. Rev. A* 2011, 84, 023813.

(22) Akahane, Y.; Asano, T.; Song, B.-S.; Noda, S. High-Q Photonic Nanocavity in a Two-Dimensional Photonic Crystal. *Nature* 2003, 425, 944−947.

(23) Taton, T. A.; Norris, D. J. Device Physics: Defective Promise in Photonics. *Nature* 2002, 416, 685−686.

(24) Vekris, E.; Kitaev, V.; von Freymann, G.; Perovic, D. D.; Aitchison, J. S.; Ozin, G. A. Buried Linear Extrinsic Defects in Colloidal Photonic Crystals. *Adv. Mater.* 2005, 17, 1269−1272.

(25) Yan, Q.; Zhou, Z.; Zhao, X. S.; Chua, S. J. Line Defects Embedded in Three-Dimensional Photonic Crystals. *Adv. Mater.* 2005, 17, 1917−1920.

(26) Zhao, Y.; Wostyn, K.; de Schaetzen, G.; Clays, K.; Hellemans, L.; Persoons, A.; Szekeres, M.; Schoonheydt, R. A. The Fabrication of Photonic Band Gap Materials with a Two-Dimensional Defect. *Appl. Phys. Lett.* 2003, 82, 3764−3766.

(27) Massé, P.; Vallée, R. A. L.; Dechézelles, J.-F.; Rosselgong, J.; Cloutet, E.; Cramail, H.; Zhao, X. S.; Ravaine, S. Effects of the Position of a Chemically or Size-Induced Planar Defect on the Optical Properties of Colloidal Crystals. *J. Phys. Chem. C* 2009, 113, 14487−14492.

(28) Rengarajan, R.; Jiang, P.; Larrabee, D. C.; Colvin, V. L.; Mittleman, D. M. Colloidal Photonic Superlattices. *Phys. Rev. B* 2001, 64, 205103.

(29) Egen, M.; Voss, R.; Griesebock, B.; Zentel, R.; Romanov, S.; Torres, C. S. Heterostructures of Polymer Photonic Crystal Films. *Chem. Mater.* 2003, 15, 3786−3792.

(30) Hwang, D.-K.; Noh, H.; Cao, H.; Chang, R. P. H. Photonic Bandgap Engineering with Inverse Opal Multistacks of Different Refractive Index Contrasts. *Appl. Phys. Lett.* **2009**, *95*, 091101.

(31) Song, B.-S.; Noda, S.; Asano, T.; Akahane, Y. Ultra-High-Q Photonic Double-Heterostructure Nanocavity. *Nat. Mater.* **2005**, *4*, 207−210.

(32) Istrate, E.; Sargent, E. H. Photonic Crystal Heterostructures— Resonant Tunnelling, Waveguides and Filters. *J. Opt A: Pure Appl. Opt.* **2002**, *4*, S242.

(33) Ding, B.; Bardosova, M.; Povey, I.; Pemble, M. E.; Romanov, S. G. Engineered Light Scattering in Colloidal Photonic Heterocrystals. *Adv. Funct. Mater.* **2010**, *20*, 853−860.

(34) Tao, C.-a.; Zhu, W.; An, Q.; Li, G. Theoretical Demonstration of Efficiency Enhancement of Dye-Sensitized Solar Cells with Double-Inverse Opal as Mirrors. *J. Phys. Chem. C* **2010**, *114*, 10641−10647.

(35) Baert, K.; Song, K.; Vallée, R. A. L.; Van der Auweraer, M.; Clays, K. Spectral Narrowing of Emission in Self-Assembled Colloidal Photonic Superlattices. *J. Appl. Phys.* **2006**, *100*, 123112.

(36) Dechézelles, J. F.; Mialon, G.; Gacoin, T.; Barthou, C.; Schwob, C.; Maître, A.; Vallée, R. A. L.; Cramail, H.; Ravaine, S. Inhibition and Exaltation of Emission in Layer-Controlled Colloidal Photonic Architectures. *Colloids Surf. Physicochem. Eng. Aspects* **2011**, *373*, 1−5.

(37) Di Stasio, F.; Berti, L.; Burger, M.; Marabelli, F.; Gardin, S.; Dainese, T.; Signorini, R.; Bozio, R.; Comoretto, D. Amplified Spontaneous Emission from Opal Photonic Crystals Engineered with Structural Defects. *Phys. Chem. Chem. Phys.* **2009**, *11*, 11515−11519.

(38) Kim, S.-H.; Lee, S. Y.; Yang, S.-M.; Yi, G.-R. Self-Assembled Colloidal Structures for Photonics. *NPG Asia Mater.* **2011**, *3*, 25−33.

(39) Stein, A.; Wilson, B. E.; Rudisill, S. G. Design and Functionality of Colloidal-Crystal-Templated Materials-Chemical Applications of Inverse Opals. *Chem. Soc. Rev.* **2013**, *42*, 2763−2803.

(40) Gaponik, N.; Eychmüller, A.; Rogach, A. L.; Solovyev, V. G.; Sotomayor Torres, C. M.; Romanov, S. G. Structure-Related Optical Properties of Luminescent Hetero-Opals. *J. Appl. Phys.* **2004**, *95*, 1029−1035.

(41) Cai, Z.; Liu, Y. J.; Teng, J.; Lu, X. Fabrication of Large Domain Crack-Free Colloidal Crystal Heterostructures with Superposition Bandgaps Using Hydrophobic Polystyrene Spheres. *ACS Appl. Mater. Interfaces* **2012**, *4*, 5562−5569.

(42) Yan, Q.; Teh, L. K.; Shao, Q.; Wong, C. C.; Chiang, Y.-M. Layer Transfer Approach to Opaline Hetero Photonic Crystals. *Langmuir* **2008**, *24*, 1796−1800.

(43) Chen, G.; Yang, C.; Prasad, P. N. Nanophotonics and Nanochemistry: Controlling the Excitation Dynamics for Frequency Up- and Down-Conversion in Lanthanide-Doped Nanoparticles. *Acc. Chem. Res.* **2013**, *46*, 1474−1486.

(44) Anuja, D.; Amitava, P. Bright White Light Emission from In$_2$S$_3$: Eu^{3+} Nanoparticles. *J. Phys. D: Appl. Phys.* **2009**, *42*, 145116.

(45) Jeevan, M. M.; William, M. C.; May, P. S.; QuocAnh, L.; Grant, A. C.; Jon, J. K. Security printing of covert quick response codes using upconverting nanoparticle inks. *Nanotechnology* **2012**, *23*, 395201.

(46) Downing, E.; Hesselink, L.; Ralston, J.; Macfarlane, R. A Three-Color, Solid-State, Three-Dimensional Display. *Science* **1996**, *273*, 1185−1189.

(47) Scheps, R. Upconversion Laser Processes. *Prog. Quant. Electron.* **1996**, *20*, 271−358.

(48) Huang, X.; Han, S.; Huang, W.; Liu, X. Enhancing Solar Cell Efficiency: The Search for Luminescent Materials as Spectral Converters. *Chem. Soc. Rev.* **2013**, *42*, 173.

(49) Sivakumar, S.; Diamente, P. R.; van Veggel, F. C. Silica-Coated Ln^{3+}-Doped LaF$_3$ Nanoparticles as Robust Down-and Upconverting Biolabels. *Chem.—Eur. J.* **2006**, *12*, 5878−5884.

(50) Lal, S.; Link, S.; Halas, N. J. Nano-Optics from Sensing to Waveguiding. *Nat. Photonics* **2007**, *1*, 641−648.

(51) Eliseeva, S. V.; Banzli, J.-C. G. Lanthanide Luminescence for Functional Materials and Bio-Sciences. *Chem. Soc. Rev.* **2010**, *39*, 189.

(52) Romanov, S. G.; Fokin, A. V.; De La Rue, R. M. Eu^{3+} Emission in an Anisotropic Photonic Band Gap Environment. *Appl. Phys. Lett.* **2000**, *76*, 1656−1658.

(53) Zhu, Y.; Xu, W.; Zhang, H.; Wang, W.; Tong, L.; Xu, S.; Sun, Z.; Song, H. Highly Modified Spontaneous Emissions in YVO$_4$:Eu^{3+} Inverse Opal and Refractive Index Sensing Application. *Appl. Phys. Lett.* **2012**, *100*, 081104.

(54) Liu, Z.; Yang, Z.; Sun, L.; Li, B.; Zhou, J. Energy Transfer Enhancement in Eu^{3+}, Tb^{3+}-Doped SiO$_2$ Inverse Opal Photonic Crystals. *J. Am. Ceram. Soc.* **2011**, *94*, 2731−2734.

(55) Zhu, Y.; Sun, Z.; Yin, Z.; Song, H.; Xu, W.; Wang, Y.; Zhang, L.; Zhang, H. Self-Assembly, Highly Modified Spontaneous Emission and Energy Transfer Properties of LaPO$_4$:Ce^{3+}, Tb^{3+} Inverse Opals. *Dalton Trans.* **2013**, *42*, 8049−8057.

(56) Míguez, H.; Meseguer, F.; López, C.; Mifsud, A.; Moya, J. S.; Vázquez, L. Evidence of FCC Crystallization of SiO$_2$ Nanospheres. *Langmuir* **1997**, *13*, 6009−6011.

(57) Woodcock, L. V. Entropy Difference between the Face-Centred Cubic and Hexagonal Close-Packed Crystal Structures. *Nature* **1997**, *385*, 141−143.

(58) Kubrin, R.; Lee, H. S.; Zierold, R.; Yu. Petrov, A.; Janssen, R.; Nielsch, K.; Eich, M.; Schneider, G. A. Stacking of Ceramic Inverse Opals with Different Lattice Constants. *J. Am. Ceram. Soc.* **2012**, *95*, 2226−2235.

(59) Jiang, P.; Ostojic, G. N.; Narat, R.; Mittleman, D. M.; Colvin, V. L. The Fabrication and Bandgap Engineering of Photonic Multilayers. *Adv. Mater.* **2001**, *13*, 389−393.

(60) Khunsin, W.; Romanov, S. G.; Sotomayor Torres, C. M.; Ye, J.; Zentel, R. Optical Transmission in Triple-Film Hetero-Opals. *J. Appl. Phys.* **2008**, *104*, 013527.

(61) Reynolds, A.; López-Tejeira, F.; Cassagne, D.; J. García-Vidal, F.; Jouanin, C.; Sánchez-Dehesa, J. Spectral Properties of Opal-Based Photonic Crystals having a SiO$_2$ Matrix. *Phys. Rev. B* **1999**, *60*, 11422−11426.

(62) Ródenas, A.; Zhou, G.; Jaque, D.; Gu, M. Rare-Earth Spontaneous Emission Control in Three-Dimensional Lithium Niobate Photonic Crystals. *Adv. Mater.* **2009**, *21*, 3526−3530.

(63) Ning, H.; Mihi, A.; Geddes, J. B.; Miyake, M.; Braun, P. V. Radiative Lifetime Modification of LaF$_3$:Nd Nanoparticles Embedded in 3D Silicon Photonic Crystals. *Adv. Mater.* **2012**, *24*, OP153−OP158.

(64) Liu, X.-D.; Wang, Y.-Q.; Cheng, B.-Y.; Zhang, D.-Z. Conservative Form of The Density of States of a Photonic Crystal with a Pseudogap. *Phys. Rev. E* **2003**, *68*, 036610.

(65) Smith, T.; Guild, J. The C.I.E. Colorimetric Standards and their Use. *Trans. Opt. Soc.* **1931**, *33*, 73.

(66) Lakowicz, J. R. *Principles of Fluorescence Spectroscopy*, 3rd ed; Springer Science & Business Media: New York, 2007.

(67) Zhu, Y.; Xu, W.; Zhang, H.; Wang, W.; Xu, S.; Song, H. Inhibited Long-Scale Energy Transfer in Dysprosium Doped Yttrium Vanadate Inverse Opal. *J. Phys. Chem. C* **2011**, *116*, 2297−2302.

(68) Bechger, L.; Lodahl, P.; Vos, W. L. Directional Fluorescence Spectra of Laser Dye in Opal and Inverse Opal Photonic Crystals. *J. Phys. Chem. B* **2005**, *109*, 9980−9988.

(69) Meltzer, R. S.; Feofilov, S. P.; Tissue, B.; Yuan, H. B. Dependence of Fluorescence Lifetimes of Y$_2$O$_3$:Eu^{3+} Nanoparticles on the Surrounding Medium. *Phys. Rev. B* **1999**, *60*, R14012−R14015.

■ NOTE ADDED AFTER ASAP PUBLICATION

This paper was published on the Web on June 1, 2015, with minor errors in Tables 1 and 2. The corrected version was reposted on June 10, 2015.